



Reconstruction and Calibration of Contactless Electroluminescence Images From Laser Line Scanning of Photovoltaic Modules

Mantel, Claire; Benatto, Gisele Alves dos Reis; Lancia, Adrian Alejo Santamaria; Spataru, Sergiu; Poulsen, Peter Behrendorff; Forchhammer, Søren

Published in:
IEEE Journal of Photovoltaics

Link to article, DOI:
[10.1109/JPHOTOV.2022.3151327](https://doi.org/10.1109/JPHOTOV.2022.3151327)

Publication date:
2022

Document Version
Peer reviewed version

[Link back to DTU Orbit](#)

Citation (APA):
Mantel, C., Benatto, G. A. D. R., Lancia, A. A. S., Spataru, S., Poulsen, P. B., & Forchhammer, S. (2022). Reconstruction and Calibration of Contactless Electroluminescence Images From Laser Line Scanning of Photovoltaic Modules. *IEEE Journal of Photovoltaics*, 12(3), 696 - 702. Article 9736329. <https://doi.org/10.1109/JPHOTOV.2022.3151327>

General rights

Copyright and moral rights for the publications made accessible in the public portal are retained by the authors and/or other copyright owners and it is a condition of accessing publications that users recognise and abide by the legal requirements associated with these rights.

- Users may download and print one copy of any publication from the public portal for the purpose of private study or research.
- You may not further distribute the material or use it for any profit-making activity or commercial gain
- You may freely distribute the URL identifying the publication in the public portal

If you believe that this document breaches copyright please contact us providing details, and we will remove access to the work immediately and investigate your claim.

Reconstruction and Calibration of Contactless Electroluminescence Images From Laser Line Scanning of Photovoltaic Modules

Claire Mantel ¹, Associate Member, IEEE, Gisele Alves dos Reis Benatto ¹, Adrian Alejo Santamaria Lancia ¹, Sergiu Spataru ¹, Member, IEEE, Peter Behrendorff Poulsen ¹, and Søren Forchhammer ¹, Member, IEEE

Abstract—This article presents image processing methods for reconstructing and calibrating contactless electroluminescence (EL) images acquired with laser line scanning for diagnostic of photovoltaic modules. The method specifically focuses on two outputs: a contactless conventional EL that is calibrated to correspond to electrically biased EL and a contactless highlighted EL that emphasizes visualization of defects. Results are evaluated first by visual inspection, showing similar resolution to electrically biased EL at 2% or 5% Isc. A quantitative analysis by peak signal to noise ratio (PSNR) measures also assesses the resemblance between the reconstructed contactless conventional EL and the reference electrically biased EL.

Index Terms—Contactless EL (CEL), diagnostic, electroluminescence (EL), imaging, laser induced luminescence.

I. INTRODUCTION

A COMBINATION of drastic decrease of the price of photovoltaic (PV) modules (by a factor of 15 in the past 10 years [1]) and stronger focus toward renewable energy sources has led the worldwide installed capacity to a sustained growth in the past and forecasted for the coming period [2]. In order to increase the duration of the lifetime and therefore also yield of PV modules, quality control methods are necessary. The International Energy Agency established an overview of the various failures occurring in PV modules and the different modalities to detect and characterize them [3]. The need for in-field inspections of PV modules has especially driven development and progress of image-based diagnostic tools such as electroluminescence (EL) [4]–[6]. As traditional EL required biasing the imaged modules, it implies a constraining setup that slows down the diagnostic process. To address this major issue of electrically biased EL (EBEL), a way to obtain EL images without physical contact to the PV cell, named contactless EL (CEL), has been demonstrated [7], [8]. CEL is based on illuminating one part of a

PV cell while imaging another part, then moving the illumination source so that all areas of the cell are imaged while not being illuminated. It, therefore, necessitates processing of the acquired images to recreate a single image from the stack of images acquired. The acquisition method and setup used in this article was presented in [9]. It consists of a laser line that scans a whole module while an InGaAs camera acquires images continuously. This article presents the image processing methods developed to obtain useful images for PV module diagnostics using the acquisition method from [9]. The two aims of the processing are to reconstruct an image similar to the usually obtained EBEL (which acts then as a reference) and to facilitate visualization of defects in PV modules. The second goal is achieved through the production of an image that we named contactless highlighted EL (CHEL) that emphasizes defects. The creation of an image named contactless conventional EL (CCEL), that corresponds to usually obtained EBEL, requires an additional step of calibration to compensate for power variation along the laser line. The rest of this article is organized as follows. First the related literature is presented in Section II, then the methods used to reconstruct and calibrate images are presented in Section III and their performance evaluated in Section IV. Finally, Section V concludes this article.

II. PREVIOUS WORK

The main techniques for image-based diagnostic of PV modules [10] are infrared thermography (IR [11], [12]), electroluminescence (EL [4]), and photoluminescence (PL [13]). The low spatial resolution of infrared thermography makes it ill-suited to detect cracks, especially those with lower impact on power loss such as the modes A and B [14]. Luminescence imaging leverages the relation between PV quantum efficiency and luminescent emission by imaging the luminescence produced by a cell or module in answer to uniform carrier injection. In the case of EL, the uniform carrier injection is usually achieved electrically by applying forward bias current [4]. For PL, the module is illuminated from a light source, most commonly LED or laser [13]. Despite PL having the advantage over electrically biased EL of being contactless, its requirement for a uniform illumination implies a heavy light source setup, although, it has been demonstrated in outdoor conditions [15]. Some limitations of EL have since been addressed to allow, e.g., daylight outdoor operation [5], [16] through acquisition of several images to achieve a better image quality or faster image acquisition using drones [6].

Manuscript received December 9, 2021; revised January 24, 2022; accepted February 2, 2022. This work was supported in part by the DronEl2 project under EUDP - Energy Technology Development and Demonstration Program of the Danish Energy Agency under Grant 64019-0603. (Corresponding author: Claire Mantel.)

The authors are with the Department of Photonics Engineering, Denmark Technical University, 2800 Kgs. Lyngby, Denmark (e-mail: clma@fotonik.dtu.dk; garb@fotonik.dtu.dk; aasl@fotonik.dtu.dk; sersp@fotonik.dtu.dk; ppou@fotonik.dtu.dk; sofo@fotonik.dtu.dk).

Color versions of one or more figures in this article are available at <https://doi.org/10.1109/JPHOTOV.2022.3151327>.

Digital Object Identifier 10.1109/JPHOTOV.2022.3151327

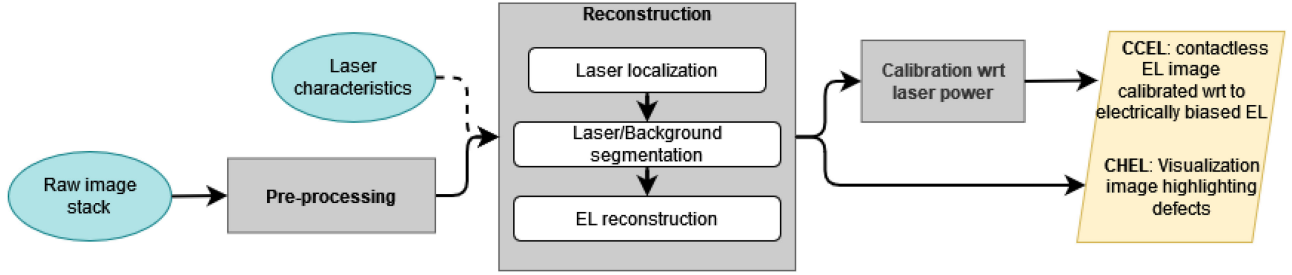


Fig. 1. Global flowchart of the method.

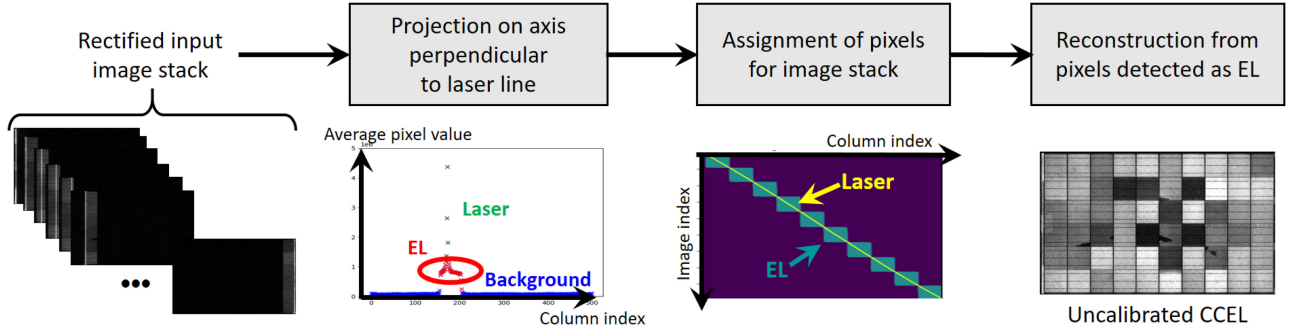


Fig. 2. Reconstruction of EL image from LIL data.

Image-based diagnostic methods require preprocessing steps such as camera calibration [17] or perspective correction [18]. To achieve the final aim of failure detection and analysis, various methods have been considered: statistical analysis [19], feature-based machine learning [20], [21], and more recently deep learning [22]–[24].

To address a major limitation of electrically biased EL imaging, i.e., the need for forward biasing the module being imaged, CEL was demonstrated in [7]. A PV cell is partially illuminated with a PL setup (790 nm laser with photon flux density comparable to 1 sun at 1.5 A.M. conditions). By shading part of it on both sides of the bus bars, they allow the creation of lateral current flow, so the shaded parts acts as current sinks and their images correspond to an EL image. That technique was further developed with a more localized LED illumination and imaged with both Si CDD and InGaAs cameras in [8] in which spatially resolved images of cracks were obtained. In [25], the influence of the shapes (full area, patterned, and scanning) and photon density of the illumination on the resulting images were studied. The characteristics of defects visualized via line scan illumination for both PL and EL are compared in [26], showing the best mode depends on the type of defects evaluated, e.g., isolated regions formed by cracks are much more easily identifiable by EL. Spatially resolved CEL imaging using laser-line scanning is demonstrated in [9], allowing identification of defects such as finger failures, areas with high series resistance or disconnected cell cracks. This article is a continuation of the method presented in [9] and the setup used in this article is the same laser-line scanning controlled by a robotic arm. Specifically, the contribution of this article is the processing of the acquired images.

- 1) We setup a partly automatic process controlled through a few parameters (whereas previous publications presented results obtained with manual control).

- 2) The calibration step allows obtaining results closer to usual electrically biased EL.

Our method produces two output images: a contactless conventional EL (CCEL) that is calibrated toward EBEL and a contactless highlighted EL (CHEL) that emphasizes the visualization of defects.

III. METHOD FOR IMAGE PROCESSING

This section presents the process used to reconstruct a few images based on the whole stack of images resulting from CEL acquisition based on laser illumination. The global pipeline is illustrated in Fig. 1. It consists of three steps going from the acquired image stack $I_{x,y,t}$ with x and y the pixel column and line index, respectively, and $t \in N$ the index of the image in the stack, to the output CCEL and CHEL images. First, the stack of raw images are preprocessed to correct for the major acquisition issues. Then, each pixel in each image of the stack is classified as either background, EL, or laser pixel and two images are reconstructed using the pixels classified as EL: one uncalibrated CCEL, corresponding to the reference EBEL and one CHEL that highlights the defects. Finally, the uncalibrated CCEL image can be calibrated into a CCEL to match the EBEL better.

A. Preprocessing

The aim of the preprocessing step is to correct for issues that arise during the acquisition process. The two issues handled here are namely the correction of false pixel values because of defective pixels and the correction of the distortion because of perspective.

Defective pixels in a sensor can occur both during manufacturing and operation and manifest in pixels at some fixed locations yielding values not accurately representing the scene

imaged. These defects are commonly adjusted to a more correct value through software processing. The first step toward the restoration of those defective pixels is to identify their location. We assume here that no new defective pixel occurs during a sequence acquisition so the localization process is done using the first image of the sequence $I_{x,y,0}$, for which the laser has not started activating the panel yet and all pixels should therefore be background/dark pixels. We then identify defective pixels as those having a too high luminance value. $I_{x,y,0}$ is first filtered by a 5×5 median filter: $BI_{x,y,0}$ and the difference $D_{x,y,0}$ between $I_{x,y,0}$ and $BI_{x,y,0}$ is computed. The pixels of $D_{x,y,0}$ having a higher value than a specified threshold (fixed at half of the camera dynamic range here) are considered as defective and their coordinates stored. For all N images from the stack, the values at those coordinates are replaced by the result of a median filter on a 5×5 neighborhood.

The perspective correction is handled using the method presented by Mantel *et al.* [18]. This process also allows an image to be obtained for which the whole area is occupied by the PV panel and the coordinates of the corners of each cells.

B. Reconstruction

The aim of this section is to reconstruct two images based on the whole stack of images acquired via laser-based CEL. It assumes that the input images have been corrected for perspective correction and that the panel occupies the whole image area. The full process is illustrated in Fig. 2.

The reconstruction is done in two steps: first in each image of the stack, the location of the laser line is determined and the image is segmented in three regions: background, EL, and laser. The second step of the reconstruction is to combine the pixels classified as EL into two images: one uncalibrated CCEL, corresponding to EBEL and one CHEL that highlights the defects.

1) *Laser Retrieval and Segmentation*: The first region contains background pixels, i.e., those corresponding to the parts of the panel that are not activated and therefore barely visible to the camera. The second region contains EL pixels, which correspond to areas for which the laser is illuminating the cell but not the area itself. Finally, the third region contains the pixels corresponding to areas where the laser is incident.

The detection of the regions borders is achieved via the projection of each image in the direction perpendicular to the laser scanning direction. In Fig. 2, for images acquired with a horizontal laser scanning, the projection is performed per column. The projection allows the simplification of the data to handle (1-D instead of 2-D) and attenuates part of the image noise by averaging it over a full column (or row).

The projections are then sorted to classify them. The number of columns classified as nonbackground (i.e., EL + laser) are determined by the ratio R between the number of columns in the image and the panel. The columns having the R highest values are classified as EL + laser and the rest as background. The width of the laser beam is a fixed parameter.

2) *Image Reconstruction*: The uncalibrated CCEL is obtained by applying a median filter in the time dimension of the image stack $I_{x,y,t}$, which, as studied in [27], provides a satisfying result for multiple images of the same scene that are well registered. The CHEL aims at capturing highlighted defects. As illustrated in [9], it arises when the laser hits an isolated area such that the ratio between the power received and the size of the isolated area lead to higher EL level than that of a

well functioning cell. For that purpose the pixels are sorted and those at the Th_{CHEL} highest percentiles are selected to form an image.

C. Calibration of CCEL Image Toward a Reference EL

The aim of this step is to adjust the values of the uncalibrated CCEL to represent similar information to that of EBEL. The need for this calibration comes from the variation in power observed along the laser line, measured up to 40%. Those variations yield in turn variations in the EL produced by each cell of the panel and, therefore, pixel values when those are imaged.

The process is illustrated in Fig. 3. The model takes as input the median of pixel values within each cell of the uncalibrated CCEL, noted $UCCEL_{C_{i,j}}$ for the cell at index (i, j) , and some information characterizing the laser and outputs predictions of $EBEL_{C_{i,j}}$, the median of the cell values of the EBEL image at 2% Isc. Various regression models were considered and tried by order of complexity. The most simple model yielding satisfactory results is a second-order polynomial regression using the ordinary least squares approach (implementation from Sci-kit learn [28]). The model is first built using images from one PV panel as illustrated in Fig. 3(a) and then applied on different panel types, as illustrated in Fig. 3(b).

Initially, the regression model was given as input the measures of the laser power incident on the module measured in a grid pattern, noted $LC_{i,j}$. To simplify this approach, we aimed at estimating the laser power variation from the uncalibrated CCEL image itself. Indeed, the luminescence of the cells and thus the brightness level of the reconstructed image are the product of the laser power and the cell performance. When a large enough number of cells is imaged along the direction opposite to the scanning, the mean of the median cell value can be used to approximate the power variation along the laser line.

IV. EVALUATION

A. Data Acquisition

The acquisition setup is similar to the one presented in [9] in terms of camera, laser, and robotic arm used. The two variations in this article, are the type of modules imaged (and that they are full modules) and that we also measured the laser power for the calibration process. The equipment used are the following.

- 1) Camera: The OWL640 InGaAs camera (resolution of 640×512 and 14 b of bitdepth) from Raptor Photonics with a short-wave infrared (SWIR) low distortion sapphire lens with fixed focal length of 25 mm were used. Two camera settings were used for the acquisition: 17 ms exposure time (with 60fps framerate) and 40 ms exposure time (with 25fps).
- 2) Laser: Line-shaped laser from Osela with a wavelength of 808 nm and a diode power of 5 W.
- 3) Robotic arm: Universal Robots UR3 with a pose repeatability ± 0.03 mm. The robotic arm operated the laser line with a scanning speed of 2°/s in both horizontal and vertical scanning directions.
- 4) Panels: Three different PV panels were used. In all cases, the acquisition was performed in open circuit conditions.
 - a) APV389: PV Module Mono-Si 250 W 60 cells from Ecoprogetti srl. Images of this panel were acquired at three distances between the laser and the panel: D1: 179.5 cm, D2: 126.5 cm, and D3: 55 cm.

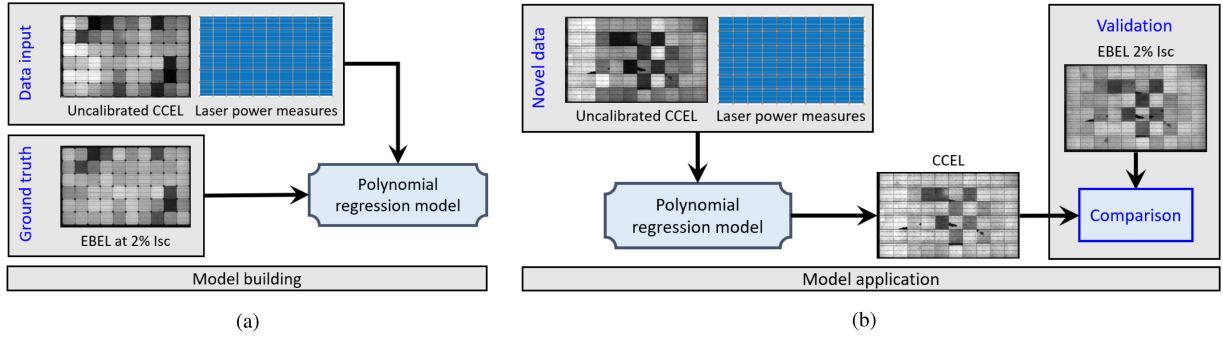


Fig. 3. Calibration process. (a) Model building. (b) Applying calibration.

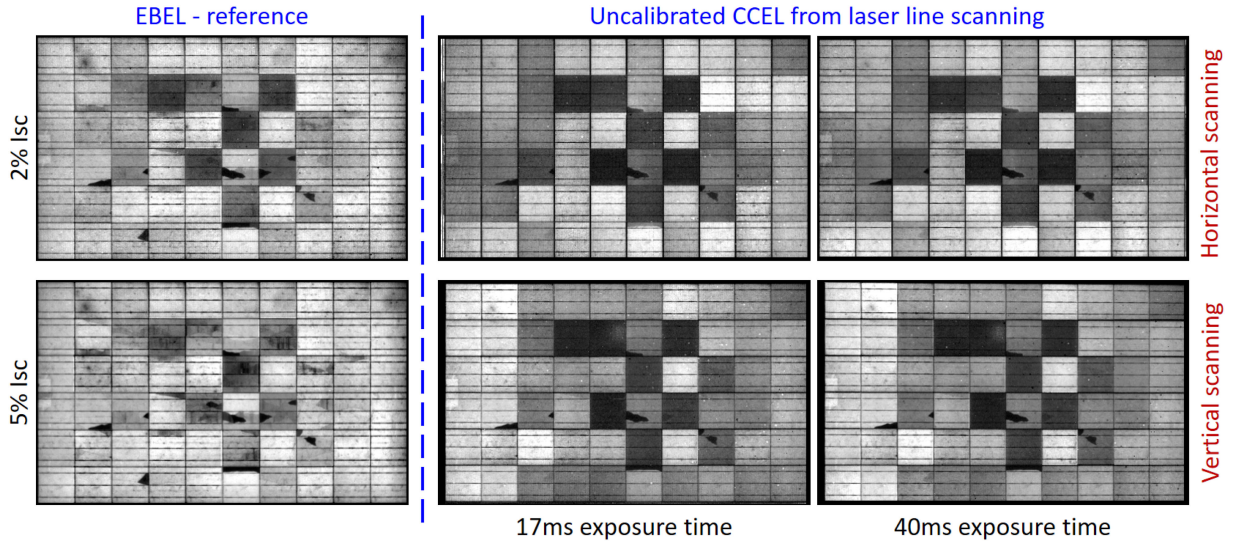


Fig. 4. Panel APV388 at D1. The leftmost column shows the reference EL images (2% Isc and 5% Isc) and the two rightmost columns the uncalibrated CCEL images reconstructed from LIL scanning. Four uncalibrated CCEL images are shown: With exposure time of 17 ms for the middle column and 40 ms for the rightmost column and with horizontal/vertical laser scanning for the top and bottom rows, respectively.

TABLE I
CHARACTERISTICS OF THE DATASETS USED

	Panel		Acquisition				# of datasets
	Model	Type	Distances	Exposure time	Scan speed	Scanning	
Model building	APV389	MonoCrystalline	D1, D2, D3	17ms (60fps)	2°/s	Hor/Vert	6
Test	APV388	PolyCrystalline	D1, D2, D3	17ms (60fps), 40ms (25fps)	2°/s	Hor/Vert	12
	APV402	MonoCrystalline	Unknown D	17ms	2°/s	Hor/Vert	2

The distances correspond to a distance between panel and laser of D1: 179.5 cm, D2: 126.5 cm, and D3: 55 cm, respectively.

- b) APV388: PV Module Multi-Si 250 W 60 cells from Ecoprogetti srl. Images of this panel were acquired at the three same distances between the laser and the panel: D1, D2, and D3.
- c) APV402: PV Module Mono-Si 4 × 9 cells black frame from MG Solar. Imaged at an unknown distance.

With regard to the model building/application scheme illustrated in Fig. 3, the panel APV389 is used to build a model [see Fig. 3(a)] that is applied on the two others panels (APV388 and APV402) as shown in Fig. 3(b).

- 5) Laser power: The power of the laser incident on the panel was measured using a laser power/energy meter from Ophir Nova. We attached to it an Ophir photodiode power sensor PD300 with filter installed.

The temperature of the room used for these experiments was controlled and monitored. The characteristics of the resulting datasets are summarized in Table I.

When we set the laser closer than D1 to the module being imaged, we also set the camera closer. In those cases (at D2 and D3), the field of view of the camera-lens system does not allow to image the full panel anymore but only some cells at the center

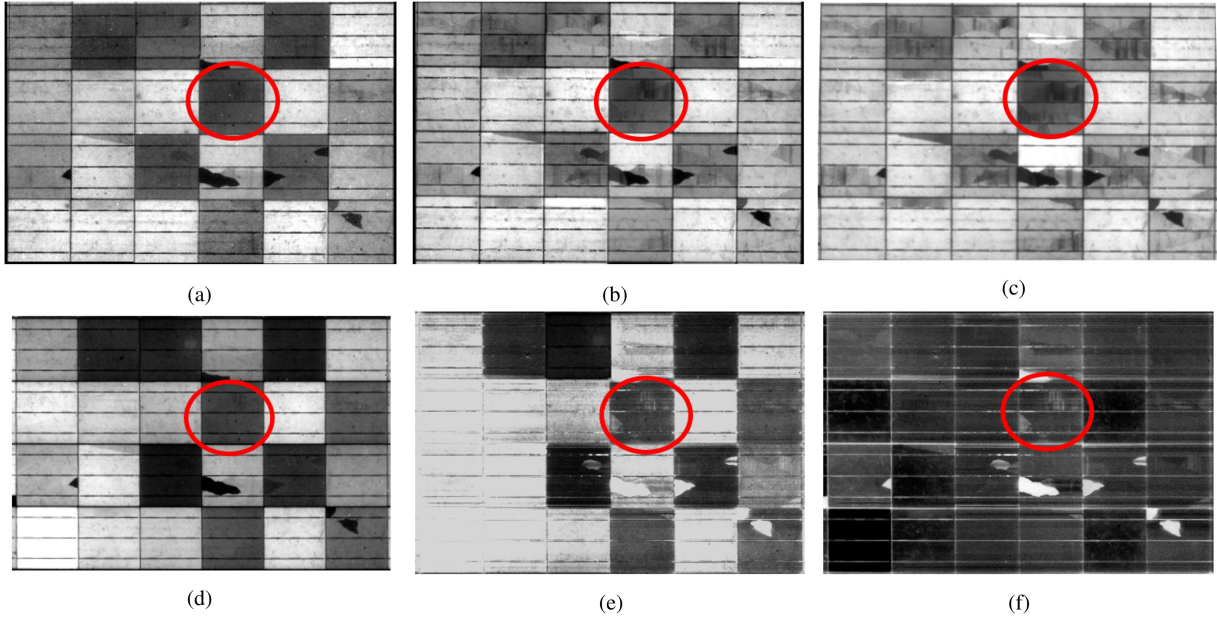


Fig. 5. Cells from panel APV388 at D2. The upper line column shows the reference EL images (2% Isc, 5% Isc, and 10% Isc) and the lower line the reconstructed images (uncalibrated CCEL, CHEL, and difference between the two). (a) Biased EL at 2% Isc (reference). (b) Biased EL at 5% Isc (reference). (c) Biased EL at 10% Isc (reference). (d) Uncalibrated CCEL from vertical scanning (40 ms exp. time). (e) Reconstructed CHEL from vertical scanning (40 ms exp. time). (f) Difference image between CHEL and CCEL.

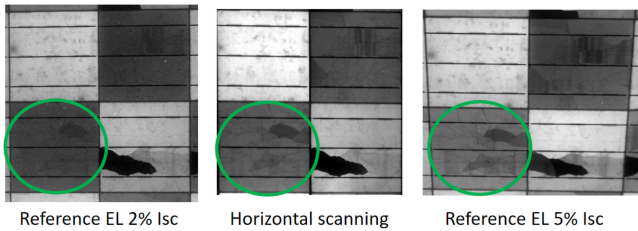


Fig. 6. Cells from panel APV388 at D3.

of the module and therefore the reconstruction at D2 and D3 provides those cells only.

B. Results for Reconstruction

Two types of reconstructed images will be evaluated in this section—the uncalibrated CCEL which aims at retrieving EBEL and the CHEL which aims at making defects more visible. The evaluation is mainly done through visual assessment and complemented by objective quality indicators measuring the fidelity of the uncalibrated CCEL to EBEL.

For the reconstruction process, the following parameters were used: the perspective correction produces images with a resolution of 50×50 pixels for the cells so the ratio R between the number of columns in the module and in the image is set at 50.

1) *Uncalibrated Contactless Conventional Electroluminescence*: The main items for evaluating the reconstruction of uncalibrated CCEL (CCEL) images is to which extent they show defects on the modules and how close to usual electrically biased EL (EBEL) they are. Results from the three distances tried, are illustrated in Figs. 4–6 for D1, D2, and D3, respectively. Along with the uncalibrated CCEL, the EBEL is shown for both 2%

Isc, 5% Isc, and 10% Isc for Fig. 5 for reference. For the three distances, the two scanning directions and the two exposure times acquired, the uncalibrated CCEL shows the major defects that yield power loss, e.g., shunted cells or mode C cracks. The less significant cracks are only visible for D3, as shown in Fig. 6.

As the power of the laser that illuminates the cells diminishes when the distance between the laser origin and the panel increases, the uncalibrated CCEL reconstructed for larger distances are closer to EBEL at lower Isc. In the case of D1 and D2, the uncalibrated CCEL is closest to the 2% Isc reference, whereas, for D3 the 5% Isc is the most similar. That effect combines with a better angular resolution of the camera at shorter distances to display more details in the uncalibrated CCEL acquired at the shortest distance (D3, shown in Fig. 6). In the IEC standard for EL imaging [14], the bias current advised for EL imaging is both low, 10% Isc, and high, 100% Isc, to allow visualizing a wide range of defects. The power of the laser used in our setup, together with the size of the area it illuminates, create similar EL irradiance to that of low current bias EL [similar defects type can be visible from 5% Isc and 10% Isc images as can be seen in Fig. 5(b) and (c), respectively]. To the best of our expectations, the method presented here would work identically with a higher irradiant laser power.

The laser orientation and scanning direction relative to the cell busbars has a significant influence on the overall pixel value of each cell, as can be seen by comparing the horizontal and vertical scanning in Fig. 4 (top and bottom lines of the LIL, respectively). That effect is because of power variations along the line of the laser and is addressed in Section IV-C.

To compare quantitatively with the EBEL, the peak signal-to-noise ratio (PSNR [29]) is used to measure the degree of resemblance between two input images. It computes on a logarithmic scale the ratio of the squared peak image value divided by the error between the reference EBEL and the uncalibrated CCEL

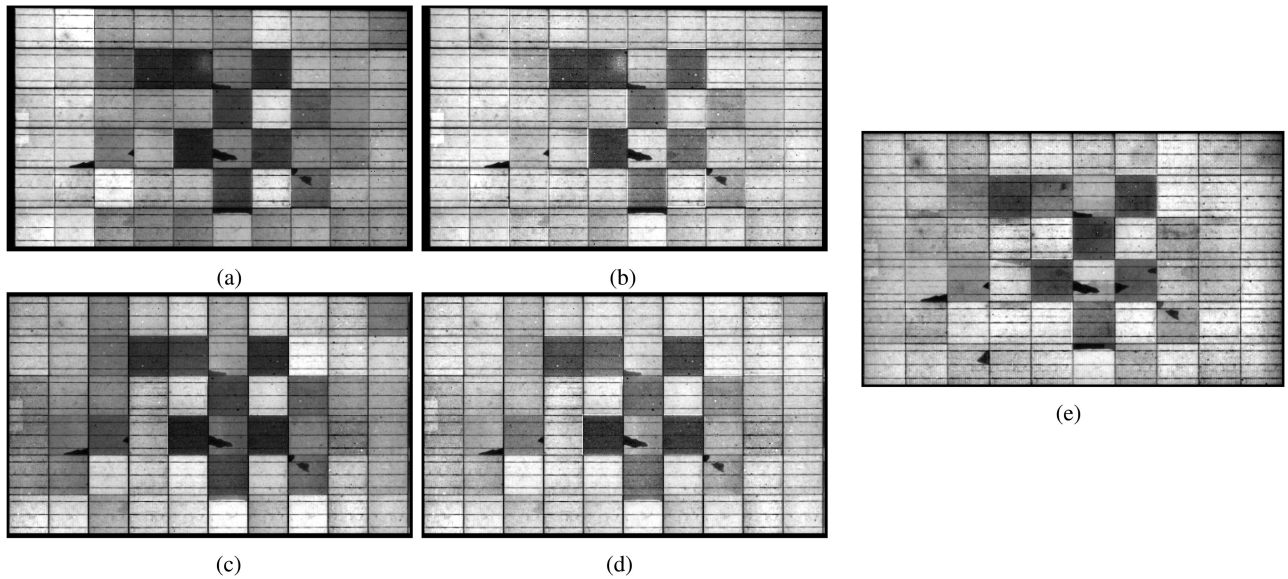


Fig. 7. Effect of calibration for CCEL reconstructed images from panel APV388 at D1. BC and AC stand for before and after calibration, respectively. (a) CCEL from vertical scanning BC. (b) CCEL from vertical scanning AC. (c) CCEL from horizontal scanning BC. (d) CCEL from horizontal scanning AC. (e) Electrically biased EL (EBEL) at 2% Isc for reference.

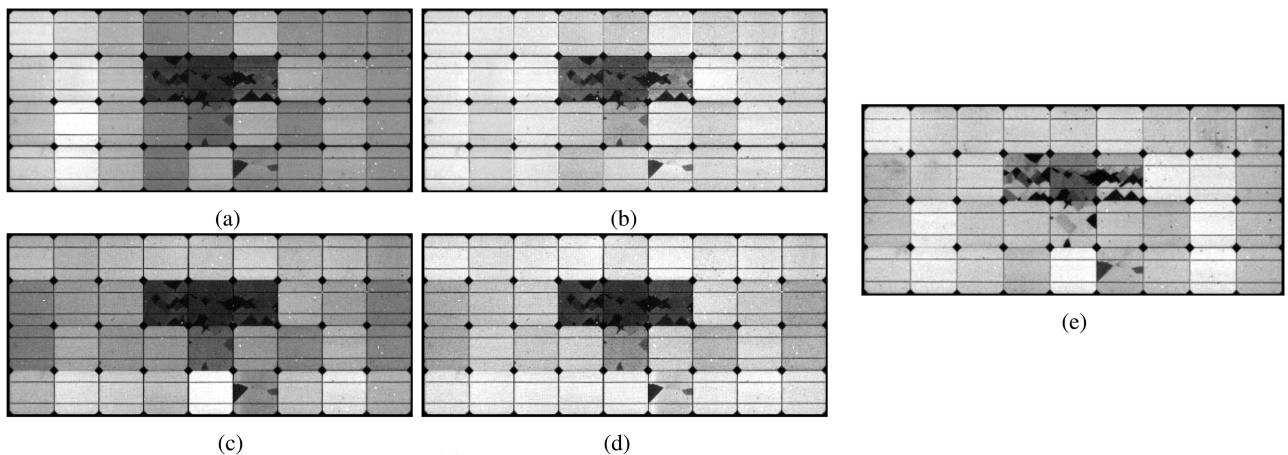


Fig. 8. Effect of calibration for CCEL reconstructed images from panel APV402 at unknown distance. BC and AC stand for before and after calibration, respectively. (a) CCEL from vertical scanning BC. (b) CCEL from vertical scanning AC. (c) CCEL from horizontal scanning BC. (d) CCEL from horizontal scanning AC. (e) Electrically biased EL (EBEL) at 2% Isc for reference.

TABLE II
ESTIMATION OF THE PERFORMANCE OF THE CALIBRATION
THROUGH PSNR ESTIMATION

Dataset		PSNR comparison with 2% Isc EL	
		BC	AC
APV388	D1, Laser measures	17.07	23.01
APV388	D1, Fr. images	17.07	23.16
APV388	D2, Laser measures	14	22
APV402	Unknown distance	18.86	22.8

BC and AC stand for before and after calibration, respectively.

on a pixel-by-pixel basis. The evaluations, given in Table II in the columns BC (before calibration), indicate a moderate

resemblance, which could stem from an imperfect pixel-to-pixel matching and the power variation along the laser line addressed in Section IV-C.

2) *Contactless Highlighted Electroluminescence*: The CHEL represent the EL of isolated areas smaller than a cell when they are illuminated by the laser, but not when the laser is directly incident on them. The incident power from the laser in an undamaged cell distributes over the whole cell surface, whereas the incident laser power in those isolated areas has less surface to distribute over, leading to a higher level of EL, and a higher pixel value in the image. One example of such a CHEL image is depicted in Fig. 5(e) for the vertical scanning of the panel APV388 with 40 ms exposure time.

One way to highlight even more those isolated areas is to compute the difference image DiffEL between the CHEL and the uncalibrated CCEL. The result of such a difference is illustrated

in Fig. 5(f). As shown in this example, removing the elements common to both CHEL and uncalibrated CCEL allows visualizing the isolated areas better but also highlights some smaller defects that are not visible in the CCEL alone, such as the small cracks circled in red in Fig. 5.

C. Results for Calibration

The evaluation of results from the calibration is done both by visual inspection and objective measures. Fig. 7 illustrates the effect of the calibration on the panel APV388 at D1. Improvement in terms of the similarity of the cell values is clearly visible both for vertical scanning [from Fig. 7(a) to (b)] and horizontal scanning [from Fig. 7(c) to (d)]. In a similar setting, Fig. 8 illustrates the effect of the model on the panel APV402, i.e., when the distance between the laser and the panel is unknown and with no laser measures.

PSNR is used to evaluate the resemblance between the reference EBEL and the reconstructed CCEL, both before and after calibration. Their results are given in Table II. Results clearly show an improvement in the fidelity because of the calibration in all cases: the PSNR is improved by +4 to +8 dB.

V. CONCLUSION

This article presents image processing methods generating two types of images from contactless EL based on laser line scanning: CCEL that corresponds to EBEL and CHEL that emphasizes defects. With the 5-W laser used in our setup, depending on the received power density (i.e., the distance between the laser line and the module), the resulting CCEL shows failures similarly to the EBEL under 2% I_{sc} or 5% I_{sc} . We also introduce a calibration method to counterbalance the non uniformity in the power density along the laser line, allowing to increase the similarity between the reconstructed CCEL and the EBEL, as measured by the increase in the objective metric PSNR.

REFERENCES

- [1] M. A. Green, "Photovoltaic technology and visions for the future," *Prog. Energy*, vol. 1, no. 1, Jul. 2019, Art. no. 13001. [Online]. Available: <https://doi.org/10.1088/2516-1083/ab0fa8>
- [2] IEA, "Renewables 2020, analysis and forecast to 2025," International Energy Agency, Paris, France, 2019. [Online]. Available: https://www.powermag.com/wp-content/uploads/2020/11/renewables_2020-pdf.pdf
- [3] M. Köntges *et al.*, "Review of failures of photovoltaic modules," Rep. IEA-PVPS T13-01:2014, Mar. 2014.
- [4] T. Fuyuki, H. Kondo, T. Yamazaki, Y. Takahashi, and Y. Uraoka, "Photographic surveying of minority carrier diffusion length in polycrystalline silicon solar cells by electroluminescence," *Appl. Phys. Lett.*, vol. 86, no. 26, 2005, Art. no. 262108. [Online]. Available: <https://doi.org/10.1063/1.1978979>
- [5] L. Stoicescu, M. Reuter, and J. Werner, "DaySy: Luminescence imaging of PV modules in daylight," in *Proc. 29th Eur. Photovolt. Sol. Energy Conf. Exhib.*, 2014, pp. 2553–2554.
- [6] G. A. d. R. Benatto *et al.*, "Drone-based daylight electroluminescence imaging of PV modules," *IEEE J. Photovolt.*, vol. 10, no. 3, pp. 872–877, May 2020.
- [7] M. Kasemann *et al.*, "Contactless qualitative series resistance imaging on solar cells," *IEEE J. Photovolt.*, vol. 2, no. 2, pp. 181–183, Apr. 2012.
- [8] S. Johnston, "Contactless electroluminescence imaging for cell and module characterization," in *Proc. IEEE 42nd Photovolt. Specialist Conf.*, 2015, pp. 1–6.
- [9] G. A. d. R. Benatto *et al.*, "Laser induced luminescence characterization of mechanically stressed PV cells," in *Proc. 48th IEEE Photovolt. Specialists Conf.*, 2021, pp. 1949–1953.
- [10] R. Ebner, B. Kubicek, and G. Újvári, "Non-destructive techniques for quality control of PV modules: Infrared thermography, electro- and photoluminescence imaging," in *Proc. 39th Annu. Conf. IEEE Ind. Electron. Soc.*, 2013, pp. 8104–8109.
- [11] C. Buerhop-Lutz, D. Schlegel, C. Vodermayr, and M. Nieß, "Quality control of PV-modules in the field using infrared-thermography," in *Proc. 26th Eur. Photovolt. Sol. Energy Conf. Exhib.*, 2011, pp. 3894–3897.
- [12] H. Straube, J.-M. Wagner, J. Schneider, and O. Breitenstein, "Quantitative evaluation of loss mechanisms in thin film solar cells using lock-in thermography," *J. Appl. Phys.*, vol. 110, no. 8, 2011, Art. no. 84513.
- [13] T. Trupke, R. A. Bardos, M. C. Schubert, and W. Warta, "Photoluminescence imaging of silicon wafers," *Appl. Phys. Lett.*, vol. 89, no. 4, 2006, Art. no. 44107, doi: [10.1063/1.2234747](https://doi.org/10.1063/1.2234747).
- [14] *Photovoltaic Devices - Part 13: Electroluminescence of Photovoltaic Modules*, IEC Standard TS 60904-13, 2018.
- [15] B. Doll *et al.*, "Photoluminescence for defect detection on full-sized photovoltaic modules," *IEEE J. Photovolt.*, vol. 11, no. 6, pp. 1419–1429, Nov. 2021.
- [16] O. Kunz, G. Rey, M. K. Juhl, and T. Trupke, "High throughput outdoor photoluminescence imaging via PV string modulation," in *Proc. IEEE 48th Photovolt. Specialists Conf.*, 2021, pp. 346–350.
- [17] K. Bedrich *et al.*, "Electroluminescence imaging of PV devices: Advanced vignetting calibration," *IEEE J. Photovolt.*, vol. 8, no. 5, pp. 1297–1304, Sep. 2018.
- [18] C. Mantel *et al.*, "Method for estimation and correction of perspective distortion of electroluminescence images of photovoltaic panels," *IEEE J. Photovolt.*, vol. 10, no. 6, pp. 1797–1802, Nov. 2020.
- [19] S. Spataru *et al.*, "Quantification of solar cell failure signatures based on statistical analysis of electroluminescence images," in *Proc. 33rd Eur. Photovolt. Sol. Energy Conf. Exhib.*, 2017, pp. 1466–1472.
- [20] C. Mantel *et al.*, "Machine learning prediction of defect types for electroluminescence images of photovoltaic panels," *Proc. SPIE*, vol. 11139, 2019, Art. no. 1113904.
- [21] S. Deitsch *et al.*, "Automatic classification of defective photovoltaic module cells in electroluminescence images," *Sol. Energy*, vol. 185, pp. 455–468, 2019. [Online]. Available: <https://doi.org/10.1016/j.solener.2019.02.067>
- [22] W. Tang, Q. Yang, K. Xiong, and W. Yan, "Deep learning based automatic defect identification of photovoltaic module using electroluminescence images," *Sol. Energy*, vol. 201, pp. 453–460, 2020. [Online]. Available: <https://www.sciencedirect.com/science/article/pii/S0038092X20302875>
- [23] M. Hoffmann *et al.*, "Deep-learning-based pipeline for module power prediction from electroluminescence measurements," *Prog. Photovolt.: Res. Appl.*, vol. 29, no. 8, pp. 920–935, 2021. [Online]. Available: <https://onlinelibrary.wiley.com/doi/abs/10.1002/ppp.3416>
- [24] U. Otamendi *et al.*, "Segmentation of cell-level anomalies in electroluminescence images of photovoltaic modules," *Sol. Energy*, vol. 220, pp. 914–926, 2021. [Online]. Available: <https://www.sciencedirect.com/science/article/pii/S0038092X21002462>
- [25] D. B. Sulas, S. Johnston, and D. C. Jordan, "Comparison of photovoltaic module luminescence imaging techniques: Assessing the influence of lateral currents in high-efficiency device structures," *Sol. Energy Mater. Sol. Cells*, vol. 192, pp. 81–87, 2019. [Online]. Available: <https://www.sciencedirect.com/science/article/pii/S0927024818305907>
- [26] I. Zafirovska, M. K. Juhl, and T. Trupke, "Comparison of line scan luminescence imaging techniques for defect characterisation in crystalline silicon solar modules," in *Proc. IEEE 7th World Conf. Photovolt. Energy Convers.*, 2018, pp. 1364–1369.
- [27] T. Buades, Y. Lou, J. M. Morel, and Z. Tang, "A note on multi-image denoising," in *Proc. Int. Workshop Local Non-Local Approximation Image Process.*, 2009, pp. 1–15.
- [28] F. Pedregosa *et al.*, "Scikit-learn: Machine learning in Python," *J. Mach. Learn. Res.*, vol. 12, pp. 2825–2830, 2011.
- [29] R. C. Gonzalez and R. E. Woods, *Digital Image Processing*, 4th ed. London, U.K.: Pearson, 2018.